Growth of double-barrier β-$(AlGa)_2O_3/Ga_2O_3$ structure and heavily Sn-doped Ga_2O_3 layers using molecular-beam epitaxy

Hironori Okumura[1*]

1 Faculty of Pure and Applied Science, University of Tsukuba, Tsukuba 305-8573 Japan

[*]E-mail: okumura.hironori.gm@u.tsukuba.ac.jp

I report on the growth of double-barrier β-$(Al_{0.15}Ga_{0.85})_2O_3/Ga_2O_3/(Al_{0.15}Ga_{0.85})_2O_3$ heterostructure and heavily Sn-doped β-Ga_2O_3 layers toward the application of resonant tunneling diodes. The Ga_2O_3 and $(AlGa)_2O_3$ layers were grown on a β-Ga_2O_3 (010) substrate by plasma-assisted molecular-beam epitaxy. The heavily Sn-doped β-Ga_2O_3 layer had a layer resistivity of 2×10^{-3} Ωcm and a specific contact resistivity of 9×10^{-6} Ωcm^{-2}. The diode with the double-barrier $(AlGa)_2O_3/Ga_2O_3/(AlGa)_2O_3$ structure sandwiched between the heavily Sn-doped Ga_2O_3 layers exhibited negative differential resistance with a peak-to-valley current ratio of 2 at room temperature.

1. Introduction

Terahertz radiations have attracted much attention for the biomedical tissue imaging, security screening, and wireless communication. Terahertz wave generation at room temperature can be achieved using resonant-tunneling diodes with the short resonant-tunneling and charging times [1, 2]. Generally, resonant-tunneling diodes consist of a quantum well sandwiched by double barriers at the conduction band using heteroepitaxy. The large conduction-band energy offset, such as AlAs/GaAs [3], AlN/GaN [4-6], and ZnMgO/ZnO systems [7, 8], is preferable to minimize thermionic currents over the barrier. I propose the new system using $(AlGa)_2O_3/Ga_2O_3$, which has the conduction-band energy discontinuity of 3.2 eV at maximum [9]. $(AlGa)_2O_3/Ga_2O_3$ resonant-tunneling diodes would provide higher operating temperatures and power output for terahertz oscillators.

Both Ga_2O_3 and Al_2O_3 single crystals have a lot of polymorphs. For Ga_2O_3, α-corundum and γ-spinel structures are meta stable [10, 11], while a monoclinic β-gallia structure is the most thermally stable [12]. Bulk β-Ga_2O_3 is commercially available at a large scale. β-Ga_2O_3 films are homoepitaxially grown by molecular-beam epitaxy (MBE), metal-organic chemical vapor epitaxy [13], and halide vaper phase epitaxy [14]. Current MBE growth of β-Ga_2O_3 uses the (010) orientation because of the practical growth rate [15]. Recently, β-$(AlGa)_2O_3/Ga_2O_3$ (010) pseudomorphical growths with small inhomogeneity and extremely flat heterointerfaces are reported using plasma-assisted (PA) MBE [16]. The abrupt heterointerface enhances the coherence of the electron wave for resonant-tunneling diodes. $(AlGa)_2O_3/Ga_2O_3$ resonant-tunneling diodes demand a heavy doping in n-type β-Ga_2O_3 emitter/collector layers to operate at a low bias voltage. Si, Sn, and Ge atoms act as donors for β-Ga_2O_3 [17-19]. However, there are few reports on a heavily doped β-Ga_2O_3 growth [20, 21].

In this paper, I report on the growth of heavily Sn-doped β-Ga_2O_3 (010) layers and a double-barrier β-$(AlGa)_2O_3/Ga_2O_3$ heterostructure, and the electrical property of the diode with the double-barrier $(AlGa)_2O_3/Ga_2O_3/(AlGa)_2O_3$ structure sandwiched between heavily Sn-doped Ga_2O_3 layers.

2. Growth of heavily Sn-doped β-Ga_2O_3 (010)

2.1. Experimental procedure

The Ga_2O_3 and $(AlGa)_2O_3$ layers were grown on Sn-doped β-Ga_2O_3 (010) substrates by PAMBE. After solvent cleaning with acetone and isopropanol, the β-Ga_2O_3 substrates were mounted on a SiC thermal-diffusion plate and were loaded into the MBE chamber with the base pressure of 1×10^{-7} Pa. The MBE system is equipped with conventional effusion cells to evaporate liquid Ga (99.9999%) and Al (99.999%), and a radio-frequency plasma cell to produce active oxygen. For the oxygen plasma source, high-purity O_2 gas (99.99995%) was supplied through a mass-flow controller. The plasma power and flow rate of oxygen was maintained at 200 W and 1.0 sccm, respectively. SnO_2 (99.99%) was used as an *n*-type doping source of β-Ga_2O_3. The doping concentration of Sn is independent on the growth temperature, unlike that of Ge [19], and the flux of a solid SnO_2 dopant is more easily controlled by the cell temperature in comparison with a metal dopant [22]. Prior to the film growth, the elemental beam equivalent pressures (BEPs) of Ga, Al, and SnO_2 were measured using a nude ion gauge located in the substrate position. The BEP of Ga was fixed at 1×10^{-5} Pa, respectively, providing the oxygen-rich regime. I consider the pyrometer temperature, which monitors the SiC susceptor, as the growth temperature. After an oxygen plasma treatment at the background pressure of 4×10^{-3} Pa at 800 °C for 10 min to remove adsorbates from the substrate surface, the Ga_2O_3 layers were grown at 700 °C at the growth rate of 7.0±0.2 nm/min. During growth, the reflection high-energy electron diffraction patterns were streaky, indicating a two-dimensional growth mode.

The root-mean-square (RMS) surface roughness of the Ga_2O_3:Sn layers was evaluated for a 2×2 μm^2 scan using atomic force microscopy. The RMS roughness of the Ga_2O_3:Sn layers was 1.3±0.2 nm for SnO_2 fluxes between 4×10^{-7} and 7×10^{-7} Pa, while the RMS roughness increased to 2.0-4.2 nm for SnO_2 fluxes between 8×10^{-7} and 3×10^{-6} Pa. The impurity concentrations of the Ga_2O_3:Sn layers were determined using secondary ion mass spectrometry performed by MST foundation. Detection limits for hydrogen, carbon, nitrogen, and tin were 3×10^{17}, 2×10^{17}, 3×10^{16}, and 9×10^{15} cm^{-3}, respectively. The net donor concentration (N_D-N_A) in the Ga_2O_3:Sn layers was determined at 1 MHz with a DC bias sweeping from −3 V to 0 V using capacitance-voltage (*C*-*V*) measurements. Layer resistivity (ρ_s) and specific contact resistivity (ρ_c) of the Ga_2O_3:Sn layers were extracted using a transfer length method (TLM) at room temperature. The ohmic contact for the *C*-*V* and TLM

measurements was obtained by Ti (20 nm)/Au (50 nm) metal stack without rapid-thermal annealing (RTA) process. The circular-anode contacts with the diameter of 100 μm were prepared for the *C-V* measurements using Ni (20 nm)/Au (50 nm) metal stacks. The rectangular electrodes with 50 μm × 100 μm patterns were arranged with the spacing between 2 and 20 μm. For high SnO_2 flux > 7×10^{-7} Pa, the capacitance was constant for the bias voltage and the resistance was not changed for the electrode distances.

2.2 Donor concentration in Sn-doped Ga_2O_3

The Sn-doping concentration [Sn] and N_D-N_A as a function of SnO_2 flux for 420-nm-thick Ga_2O_3:Sn layers are shown in Fig. 1 (a). [Sn] in the Ga_2O_3:Sn layers linearly increases with increasing the SnO_2 flux. [Sn] = 2×10^{20} cm^{-3} was independent on the growth temperatures between 600 and 750 °C. These results suggest that Sn atoms are efficiently incorporated into the Ga_2O_3 layers. N_D-N_A agrees well with [Sn] at SnO_2 flux = 4×10^{-8} Pa and increases with increasing the SnO_2 flux. For SnO_2 flux > 4×10^{-8} Pa, the difference between N_D-N_A and [Sn] increased with increasing the SnO_2 flux. The highest N_D-N_A value was 8×10^{18} cm^{-3}, which is comparable to the other reports [19, 20]. For all samples, the concentration of hydrogen, carbon, and nitrogen in the Ga_2O_3:Sn layers were under the detection limits. In the positron-annihilation spectroscopy of the Ga_2O_3:Si layers, the

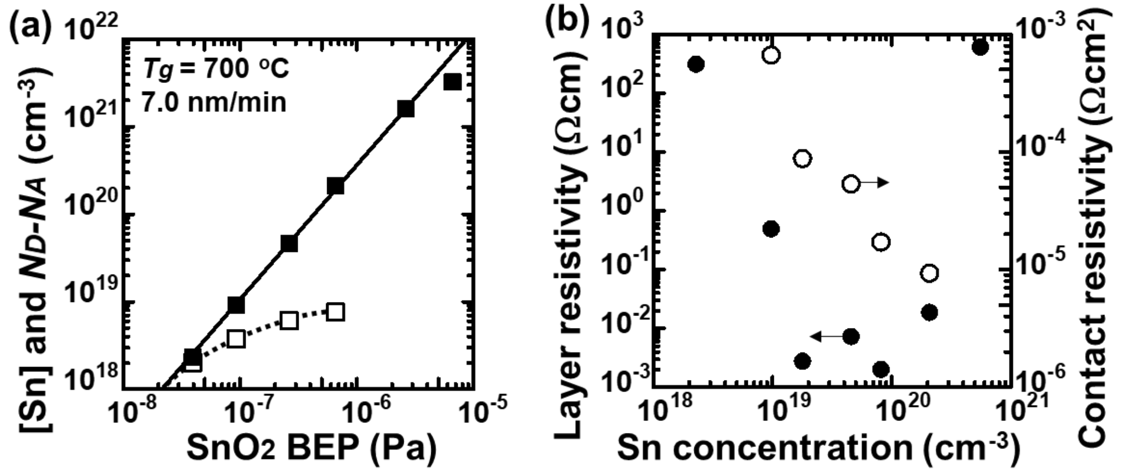

Fig. 1: (a) Sn concentration [Sn] and net donor concentration N_D-N_A dependence on SnO_2 BEP for β-Ga_2O_3:Sn (010) layers. Filled and open squares are [Sn] and N_D-N_A, respectively. (b) Layer resistivity ρ_s and contact resistivity ρ_c dependence on Sn concentrations in β-Ga_2O_3:Sn (010) layers. Filled and open circles are ρ_s and ρ_c, respectively.

gallium-vacancy concentration increases with increasing Si-donor concentration [23]. In theoretical calculation, gallium vacancy in Ga_2O_3 should be in a negative charge state for Fermi levels in the upper half of the band gap, compensating for *n*-type doping [24]. The large difference between [Sn] and N_D-N_A for the heavily Sn-doped Ga_2O_3 layers may result from the incorporation of Sn atoms into the electrically inactive site of the Ga_2O_3 layers and/or generation of the high concentration of gallium vacancy. For the further high SnO_2 flux = 7×10^{-6} Pa, the incorporation of Sn atoms into the Ga_2O_3 layers decreased, despite no additional peak in XRD. Excess Sn atoms may segregate and/or re-evaporate from the Ga_2O_3 surface. Further investigations using electron microscopy and optical measurements are necessary to clarify the behavior of excess Sn atoms in the Ga_2O_3 layers.

2.3 Electrical property of Sn-doped Ga_2O_3 layers

ρ_s and ρ_c as a function of [Sn] for 420-nm-thick Ga_2O_3:Sn layers are shown in Fig. 1 (b). In the [Sn] regimes between 2×10^{18} and 2×10^{20} cm^{-3}, I obtained ohmic behaviors without RTA process. ρ_s decreases with increasing [Sn], achieving ρ_s of 1.9 mΩcm for [Sn] = 8×10^{19} cm^{-3}. This minimum value of ρ_s is comparable to that of the Si-ion implanted Ga_2O_3 and Ge-doped Ga_2O_3 layers [17, 19]. ρ_c decreased with increasing [Sn], or N_D-N_A, thanks to high carrier-tunneling probability through the potential barrier caused by the small depletion width at the Ti/Ga_2O_3:Sn interface. The lowest ρ_c of 9×10^{-6} Ωcm^2 was achieved for [Sn] = 2×10^{20} cm^{-3}, which is comparable to ρ_c (= 5×10^{-6} Ωcm^2) of the Si-ion implanted β-Ga_2O_3 layer [17]. Both ρ_s and ρ_c dramatically increased for [Sn] > 2×10^{20} cm^{-3}, which agrees with [Sn] at the maximum N_D-N_A and [Sn] at the increased surface roughness. I suppose that the electron concentration and electron mobility in the heavily doped layers significantly decreased due to Sn-donor compensation and crystalline-quality degradation.

3. Fabrication of a diode with double-barrier β-$(AlGa)_2O_3/Ga_2O_3/(AlGa)_2O_3$ structure

3.1. Experimental procedure

The schematic structure of the diode with the symmetric double-barrier $(AlGa)_2O_3/Ga_2O_3/(AlGa)_2O_3$ structure sandwiched between heavily Sn-doped Ga_2O_3 layers is shown in Fig. 2 (a). Resonant tunneling diodes form current maxima when resonant energies for transmission through the double barriers correspond to the energy of quasi-bound states E_n in the well, followed by negative differential conductance. The current peak

is approximately obtained at the voltage $V_p \approx \frac{2E_n}{q}$ due to the bias developed across each barrier. The thick well layer reduces the ground level and V_p, and the thin barrier layer increases the peak width of longitudinal energy and the height of the resonance peak in transmission coefficient, enhancing the resonant tunneling current [3]. The larger barrier height is preferable to minimize the thermionic currents over the barrier and non-resonant tunneling current through quasi-continuum subband. Note that the Al incorporation in β-$(AlGa)_2O_3$ is limited to ~20% in PAMBE growth due to the thermodynamic equilibrium phase diagram of the Al_2O_3-Ga_2O_3 system [25, 26]. Thus, I set the practical structure of the 5-nm-thick undoped Ga_2O_3 well layer and 5-nm-thick undoped $(Al_{0.15}Ga_{0.85})_2O_3$ barrier layers.

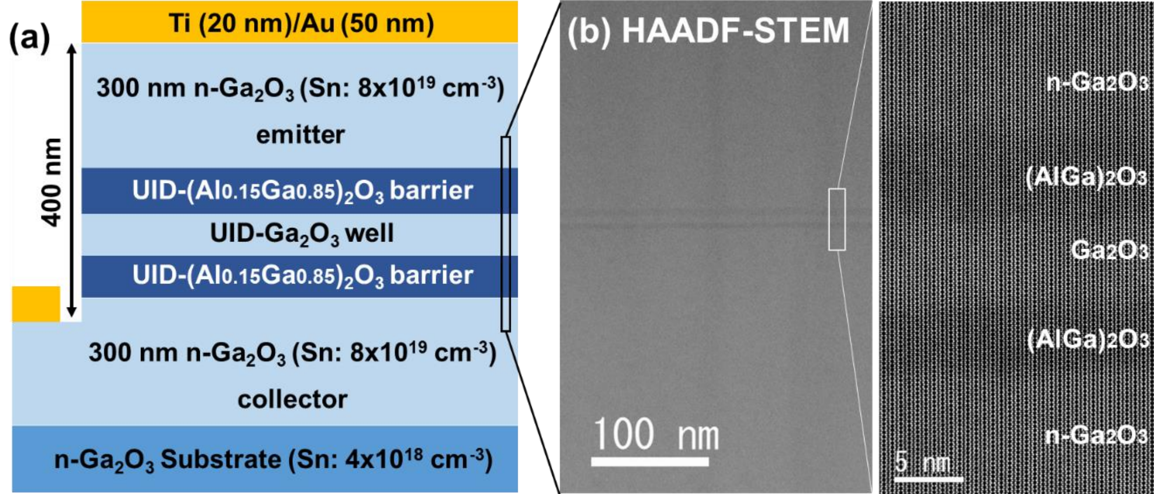

Fig. 2: (a) Schematic structure and (b) cross-sectional HAADF-STEM image of diode with double-barrier $(AlGa)_2O_3/Ga_2O_3/(AlGa)_2O_3$ structure sandwiched between heavily Sn-doped Ga_2O_3 layers.

The double-barrier $(AlGa)_2O_3/Ga_2O_3$ heterostructures were grown on a β-Ga_2O_3 (010) substrate in the oxygen-rich regime by PAMBE. The plasma power and flow rate of oxygen was maintained at 200 W and 1.0 sccm, respectively. The BEPs of Ga and Al were fixed at 1×10^{-5} and 2×10^{-6} Pa, respectively. After an oxygen plasma treatment at the background pressure of 4×10^{-3} Pa at 800 °C for 10 min to remove adsorbates from the substrate surface, the $(AlGa)_2O_3$ and Ga_2O_3 layers were grown at 700 °C at the growth rate of 7.0±0.2 nm/min. The Al composition of the $(AlGa)_2O_3$ layer was determined using peak diffraction angle from X-ray diffraction (XRD) θ-2θ scans of the (020) plane using the equation $x \cong 0.473 \times \Delta\theta_{020}$, where $\Delta\theta_{020}$ is the on-axis peak separation of the epilayer and substrate

[27]. The emitter/collector regions consist of 300-nm-thick Ga_2O_3 layers with [Sn] = 8×10^{19} cm^{-3}, which pose the minimum ρ_S. The 400-nm-deep mesa structure was fabricated by inductive-capacitance plasma (ICP) reactive-ion etching at the ICP power of 300 W with the BCl_3/Cl_2 mixing gas of 10/10 sccm [28]. Ti (20 nm) / Au (50 nm) metal stacks were deposited on the emitter/collector layers using the electron-beam evaporation. The ohmic behavior was obtained even on the etched emitter surface. The current-voltage characteristics were measured with Agilent B1500A semiconductor analyzer applying voltage sweeps between 0 and 3 V at a scan speed of 1 V/s at room temperature.

3.2. TEM observation

The cross-sectional high-angle annular dark-field (HAADF) scanning transmission-electron microscopy (STEM) image of the $(AlGa)_2O_3/Ga_2O_3$ layer with [001] azimuth, which was observed by NTT Advanced Technology Corporation, is shown in Fig. 2 (b). The clear contrast difference at the $(AlGa)_2O_3/Ga_2O_3$ interface was observed. The thicknesses of the $(AlGa)_2O_3$ emitter-barrier, Ga_2O_3 well, and $(AlGa)_2O_3$ collector-barrier layers were 6, 6, and 5 nm, respectively, close to the expected structure. The crystal structure of the $(AlGa)_2O_3$ layer follows that of the β-Ga_2O_3 layer without defects, indicating the absence of strain relaxation in the 6-nm-thick $(AlGa)_2O_3$ layer on Ga_2O_3. The Al composition in the $(AlGa)_2O_3$ barrier layer was 15 %, which was determined from the XRD θ-2θ scans. This value is close to the beam flux ratio $\phi_{Al}/(\phi_{Al}+\phi_{Ga})$ of 0.16 due to the oxygen-rich regime.

3.3 Electrical property

The current-voltage characteristic of the diode with the symmetric double-barrier $(AlGa)_2O_3/Ga_2O_3/(AlGa)_2O_3$ structure sandwiched between heavily Sn-doped Ga_2O_3 layers is shown in Fig. 3 (a). The current near the 0 V bias almost linearly increased with increasing the voltage. The first quantized level E_1 may be close to the sea of incoming electrons because of the thick well layer and heavily doped emitter layer. The diode with the diameter of 100 μm showed the clear negative-differential resistance at room temperature. If the resonant tunneling phenomenon is observed in this device, I can explain that the current peak is derived from the increase of transmission probability for electrons accumulating at the sub band adjacent to the barriers. The current peak was appeared at 2.2 V with a peak-current density of 15 kA/cm^2, which is comparable to that of the AlN/GaN system [6]. The valley current followed the sharp drop in current. The nonzero valley current results from

thermionic emission over the barrier and inelastic phonon scattering. α-and γ-Al_2O_3/Ga_2O_3 structures with the larger conduction-band energy offset would reduce the valley current [29, 30]. The peak-to-valley current ratio was ~ 2, which is comparable to or smaller than the value (= 1.5-32) of AlGaN/GaN systems [4-6, 31]. The further high peak-to-valley current ratio would be obtained by decreasing the barrier thickness and increasing Al composition in $(AlGa)_2O_3$ barrier.

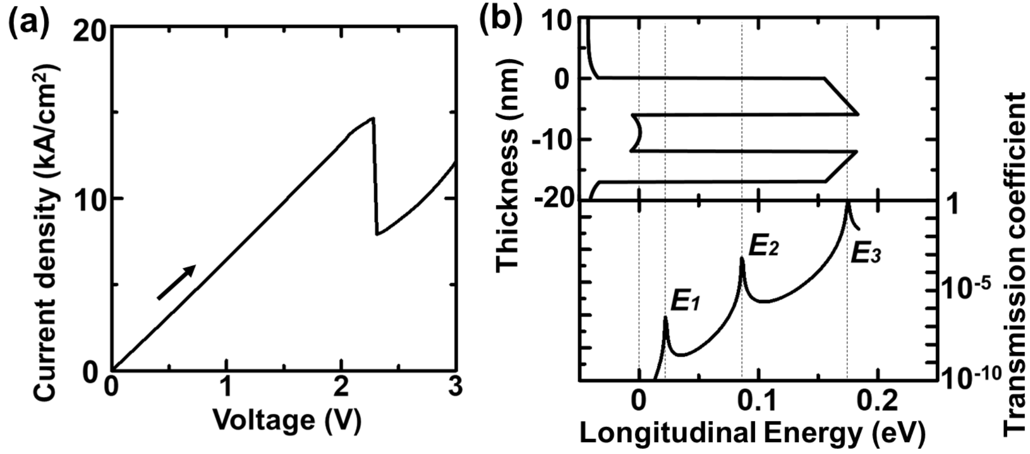

Fig. 3: (a) Current-voltage characteristics of diode with double-barrier $(AlGa)_2O_3$/Ga_2O_3/$(AlGa)_2O_3$ structure sandwiched between heavily Sn-doped Ga_2O_3 layers. (b) Energy band diagram of the double-barrier 6-nm-thick $(Al_{0.15}Ga_{0.85})_2O_3$ / 6-nm-thick Ga_2O_3 / 5-nm-thick $(Al_{0.15}Ga_{0.85})_2O_3$ structure and transmission coefficient of electron with energy through a barrier via coherent resonant tunneling.

The simulated energy band diagram of the double-barrier 6-nm-thick $(Al_{0.15}Ga_{0.85})_2O_3$ / 6-nm-thick Ga_2O_3 / 5-nm-thick $(Al_{0.15}Ga_{0.85})_2O_3$ resonant-tunneling diode based on a self-consistent solution of the Schrodinger-Poisson equation are shown in Fig. 3 (b). The conduction band energy offset ΔE_c between Ga_2O_3 and $(Al_{0.15}Ga_{0.85})_2O_3$ is estimated to be 0.18 eV using $\Delta E_c(x) = xE_{g,Al_2O_3} - xE_{g,Ga_2O_3} - bx(1-x) + x\Delta E_v$ [8], where E_{g,Al_2O_3}(= 7.24 eV) is the bandgap energy of θ-Al_2O_3, E_{g,Ga_2O_3}(= 4.87 eV) is the bandgap energy of β-Ga_2O_3, b(= 1.78 eV) is the bowing parameter for monoclinic (indirect), and ΔE_v(= 0.37 eV) is the valence-band energy offset between β-Ga_2O_3 and θ-Al_2O_3 [32]. The effective donor concentration in the UID Ga_2O_3 layer is assumed to be ~10^{17} cm^{-3} [33]. The β-$(AlGa)_2O_3$/Ga_2O_3 system without a spontaneous polarization field exhibits the symmetric band structure. The piezoelectric polarization difference between $(AlGa)_2O_3$ and Ga_2O_3 bends the conduction band in the $(AlGa)_2O_3$ barrier layer and convexs that in the thin Ga_2O_3

well layer. In the double-barrier quantum well structure, electrons are not accumulated at the barrier/well interface and can remain at quasi-bound states in the well layer. Transmission coefficient of electrons through the double barrier is calculated using $T_2 = \left(1 + \frac{4R_1}{T_1^2}\sin^2(kw - \theta)\right)^{-1}$, where R_1 ($= \frac{4E(V_0-E)}{V_0^2\sinh^2(k'l)+4E(V_0-E)}$) is the reflection probability of electrons from a single barrier, T_1 ($= 1 - R_1$) is the tunneling probability of electrons through a single barrier, k ($= \frac{\sqrt{2m^*E}}{\hbar}$) is the wave number inside the well, k' ($= \frac{\sqrt{2m^*(V_0-E)}}{\hbar}$) is the wave number upside the barrier, w is the well width, l is the barrier width, V_0 ($= \Delta E_c$) is the potential barrier height, and θ is given by $\tan\theta = \frac{2kk'}{(k^2-k'^2)\tanh(k'l)}$ [34]. Assuming that a symmetric double-barrier structure consists of 5-nm-thick $(Al_{0.15}Ga_{0.85})_2O_3$ square barriers and a 6-nm-thick Ga_2O_3 square well for simplicity, T_2 as a function of electron longitudinal energy is shown in Fig. 3 (b). The thinner barrier would increase the resonant tunneling current due to the high T_2. The calculated E_1, E_2, and E_3 are 0.022, 0.086, and 0.175 eV, respectively, indicating that the V_{p1}, V_{p2}, and V_{p3} values are 0.04, 0.17, and 0.35 V, respectively. Despite the low contact resistivity, the negative-differential resistance voltage of 2.2 V is much larger than the estimated V_p values. We speculate that the thick barrier layer and the inhomogeneity of the $(AlGa)_2O_3/Ga_2O_3$ interface increases the resonant voltage [5, 35]. In the AlN/GaN system, a defect trapping charge often causes the negative differential resistance at room temperature [36]. Typical GaN films have the dislocation density of 10^7-10^9 cm^{-2} because of the heteroepitaxial growth, resulting in the carrier trapping phenomena through dislocations. However, the β-Ga_2O_3 films have the dislocation density of ~10^3 cm^{-2} due to the homoepitaxial growth [37], indicating that the carrier trapping through dislocations is negligible for the β-Ga_2O_3 device with the diameter of 100 μm. Thus, the negative differential resistance may be attributed to electron traps related to an unintentionally incorporated silicon impurity in the $(AlGa)_2O_3$ barriers [38]. Further investigations of the temperature dependent characteristics, the current hysteresis, and the repeatability are necessary to identify the origin of the negative differential resistance.

5. Conclusion

I grew heavily Sn-doped β-Ga_2O_3 layers and double-barrier β-$(Al_{0.15}Ga_{0.85})_2O_3/Ga_2O_3$

heterostructure. The Ga_2O_3 and $(AlGa)_2O_3$ layers were grown on a β-Ga_2O_3 (010) substrate by plasma-assisted molecular-beam epitaxy. The heavily Sn-doped β-Ga_2O_3 layer had a layer resistivity of 2×10^{-3} Ωcm and a specific contact resistivity of 9×10^{-6} Ωcm^{-2}. The diode with the symmetric double-barrier $(AlGa)_2O_3/Ga_2O_3/(AlGa)_2O_3$ structure sandwiched between heavily Sn-doped Ga_2O_3 layers exhibited differential negative resistance with a peak-to-valley current ratio of 2 at room temperature.

Acknowledgements

The author would like to thank Dr. Takayoshi Oshima for his valuable suggestions. This work was financially supported by the Casio science promotion foundation, Rohm Co., Ltd., and JSPS KAKENHI Grant No. 16H06424 and was carried out with Nano-Processing Facility in the national institute of Advanced Industrial Science and Technology, and open facility in the university of Tsukuba.

References

1) M. Asada, S. Suzuki, and N. Kishimoto, Jpn. J. Appl. Phys. **47**, 4375 (2008).
2) M. Feiginov, C. Sydlo, O. Cojocari, and P. Meissner, Appl. Phys. Lett. **99**, 233506 (2011).
3) M. Tsuchiya, H. Sakaki, and J. Yoshino, Jpn. J. Appl. Phys. **24**, L466 (1985).
4) A. Kikuchi, R. Bannai, K. Kishino, C. M. Lee, and J. I. Chyl, Appl. Phys. Lett. **81**, 1729 (2002).
5) J. Encomendero, F. A. Faria, S. M. Islam, V. Protasenko, S. Rouvimov, B. S. Rodriguez, P. Fay, D. Jena, and H. G. Xing, Phys. Rev. X **7**, 041017 (2017).
6) T. A. Growden, D. F. Storm, E. M. Cornuelle, E. R. Brown, W. Zhang, B. P. Downey, J. A. Roussos, N. Cronk, L. B. Ruppalt, J. G. Champlain, P. R. Berger, and D. J. Meyer, Appl. Phys. Lett. **116**, 113501 (2020).
7) A. Ohtomo, M. Kawasaki, I. Ohkubo, H. Koinuma, T. Yasuda, and Y. Segawa, Appl. Phys. Lett. **75**, 980 (1999).
8) S. Krishnamoorthy, A. A. Iliadis, A. Inumpudi, S. Choopun, R. D. Vispute, and T. Venkatesan, Solid State Elect. **46**, 1633 (2002).
9) H. Paalaers, J. B. Varley, J. S. Speck, and C. G. Van de Walle, Appl. Phys. Lett. **112**, 242101 (2018).

10) K. Kaneko, T. Nomura, I. Kakeya, and S. Fujita, Appl. Phys. Exp. **2**, 075501 (2009).
11) T. Oshima, T. Nakazono, A. Mukai, and A. Ohtomo, J. Cryst. Growth **359**, 60 (2012).
12) T. Oshima, T. Okuno, and S. Fujita, Jpn. J. Appl. Phys. **46**, 7217 (2007).
13) F. Alema, B. Hertog, A. Osinsky, P. Mukhopadhyay, M. Toporkov, and W. V. Schoenfeld, J. Cryst, Growth **475**, 77 (2017).
14) H. Murakami, K. Nomura, K. Goto, K. Sasaki, K. Kawara, Q. T. Thieu, R. Togashi, Y. Kumagai, M. Higashiwaki, A. Kuramata, S. Yamakoshi, B. Monemar, and A. Koukitu, Appl. Phys. Exp. **8**, 015503 (2015).
15) M. Higashiwaki, K. Sasaki, A. Kuramata, T. Masui, and S. Yamakoshi, Appl. Phys. Lett. **100**, 013504 (2012).
16) S. W. Kaun, F. Wu, and J. S. Speck, J. Vac. Sci. and Tech. A **33**, 041508 (2015).
17) K. Sasakai, M. Higashiwaki, A. Kuramata, T. Masui, and S. Yamakoshi, Appl. Phys. Exp. **6**, 086502 (2013).
18) H. Okumura, M. Kita, K. Sasaki, A. Kuramata, M. Higashiwaki, and J. S. Speck, Appl. Phys. Exp. **7**, 095501 (2014).
19) E. Ahmadi, O. S. Koksaldi, S. W. Kaun, Y. Oshima, D. B. Short, U. K. Mishra, and J. S. Speck, Appl. Phys. Exp. **10**, 041102 (2017).
20) S. C. Siah, R. E. Brandt, K. Lim, L. T. Schelhas, R. Jaramilo, M. D. Heinemann, D. Chua, J. Wright, J. D. Perkins, C. U. Segre, R. G. Gordon, M. F. Toney, and T. Buonassisi, Appl. Phys. Lett. **107**, 252103 (2015).
21) M. Baldini, M. Albrecht, A. Fiedler, K. Irmscher, R. Schewski, and G. Wagner, J. Solid State Sci. and Tech. **6**, Q3040 (2017).
22) N. Kalarickal, Z. Xia, J. McGlone, S. Krishnamoorthy, W. Moore, M. Brenner, A. R. Arehart, S. A. Ringel, and S. Rajan, Appl. Phys. Lett. **115**, 152106 (2019).
23) E. Korhonen, F. Tuomisto, D. Gogova, G. Wagner, M. Maldini, Z. Galazka, R. Schewski, and M. Albrecht, Appl. Phys. Lett. **106**, 242103 (2015).
24) J. Varley, H. Peelaers, A. Janotti, and C. Van de Walle, J. Phys, Condens. Matter **23**, 334212 (2011).
25) V. G. Hill, R. Rustom, and E. F. Osborn, J. Am. Ceram. Soc. **35**, 135 (1952).
26) P. Vogt, A. Mauze, F. Wu, B. Bonof, and J. S. Speck, Appl. Phys. Exp. **11**, 115503 (2018).
27) Y. Oshima, E. Ahmadi, S. C. Badescu, F. Wu, and J. S. Speck, Appl. Phys. Lett. **9**, 061102

(2016).

28) H. Okumura and T. Tanaka, Jpn. J. Appl. Phys. **58**, 120902 (2019).

29) T. Oshima, Y. Kato, M. Imura, Y. Nakayama, and M. Takeguchi, Appl. Phys. Exp. **11**, 065501 (2018).

30) Y. Kato, M. Imura, Y. Nakayama, M. Takeguchi, and T. Oshima, Appl. Phys. Exp. **12**, 065503 (2019).

31) Z. Vashaei, C. Bayram, and M. Razeghi, J. Appl. Phys. **107**, 083505 (2010).

32) R. Zhou and R. L. Snyder, Acta Crystallogr. Sect. B Struct. Sci. **47**, 617 (1991).

33) T. Oshima, Y. Kato, N. Kawano, A. Kuramata, S. Yamakoshi, S. Fujita, T. Oishi, and M. Kasu, Appl. Phys. Exp. **10**, 035701 (2017).

34) U. K. Mishra and J. Singh, "*Semiconductor Device Physics and Design*", (Springer, 2008).

35) J. Encomendero, V. Protasenko, B. S. Rodriguez, P. Fay, F. Rana, D. Jena, and H. G. Xing, Phys. Rev. Appl. **11**, 034032 (2019).

36) S. Sakr, E. Warde, M. Tchemycheva, L. Rigutti, N. Isac, and F. H. Julien, App. Phys. Lett. **99**, 142103 (2011).

37) A. Kuramata, K. Koshi, S. Watanabe, Y. Yamaoka, T. Masui, and S. Yamakoshi, Jpn. J. Appl. Phys. **55**, 1202A2 (2016).

38) T. Oshima, Y. Kato, N. Kawano, A. Kuramata, S. Yamakoshi, S. Fujita, T. Oishi, and M. Kasu, Appl. Phys. Exp. **10**, 035701 (2017).